Study of vacancy ordering and the boson peak in metastable cubic Ge-Sb-Te using machine learning potentials

Young-Jae Choi, Minjae Ghim, and Seung-Hoon Jhi*
Department of Physics, Pohang University of Science and Technology, Pohang 37673, Republic of Korea

(Received 1 September 2023; accepted 3 January 2024; published 24 January 2024)

The mechanism of the vacancy ordering in metastable cubic Ge-Sb-Te (c-GST) that underlies the ultrafast phase-change dynamics and prominent thermoelectric properties remains elusive. Achieving a comprehensive understanding of the vacancy-ordering process at an atomic level is challenging because of enormous computational demands required to simulate disordered structures on large temporal and spatial scales. In this study, we investigate the vacancy ordering in c-GST by performing large-scale molecular dynamics simulations using machine learning potentials. The initial c-GST structure with randomly distributed vacancies rearranges to develop a semiordered cubic structure with layerlike ordered vacancies after annealing at 700 K for 100 ns. The vacancy ordering significantly affects the lattice dynamical properties of c-GST. In the initial structure with fully disordered vacancies, we observe a boson peak, usually associated with amorphous solids, that consists of localized modes at ∼0.575 THz. The boson peak modes are highly localized around specific atomic arrangements of straight vacancy-Te-vacancy trios. As vacancies become ordered, the boson peak disappears, and the Debye-Waller thermal B factor of Te decreases substantially. This finding indicates that the c-GST undergoes a transition from amorphous-like to crystalline-like solid state by thermal annealing in low-frequency dynamics.

DOI: 10.1103/PhysRevMaterials.8.013606

I. INTRODUCTION

Chalcogen-based phase-change materials are considered promising candidates for next-generation nonvolatile memory devices [1–3]. Ge-Sb-Te (GST) ternary compounds especially have attracted great attention due to the high stability of their amorphous solid phase and the convenient phase-switching operations by either electric, thermal, or laser pulses [2]. While GeTe exhibits a drastic change in resistivity (∼10^6-fold) by the amorphous-to-crystalline phase transition at $T \sim 450$ K, crystalline GST displays a multilevel resistivity spectrum over a 1000-fold range when annealed at 400 K $< T <$ 600 K [4]. Amorphous GST (a-GST) crystallizes into a metastable rocksalt cubic phase (c-GST) before further crystallizing into a hexagonal phase (h-GST). In c-GST lattice structures, anions (Te) occupy 4*a* sublattice sites, while cations (Ge/Sb) and vacancies occupy 4*b* sites [5]. Stable h-GST, obtainable by high-temperature annealing at $T >$ 500 K, has a layered structure with alternating stacks of anion and cation layers [4]. Several types of hexagonal phases are distinguished by the sequence of layer stacking, with the most stable and commonly observed being the Kooi sequence (vacancy-Te-Sb-Te-Ge-Te-Ge-Te-Sb-Te) [6].

GST phase-change memory devices exhibit fast amorphous-to-crystalline phase switching by electric pulses, which occur within 100 ns [3]. A few models have been proposed as a microscopic origin of the rapid crystallization of GST. Kolobov *et al.* proposed that the rapid phase transition of GST is possible by the facile transfer of cations from a tetrahedron center in its amorphous state to an octahedron center in its cubic state, namely the umbrella-flip distortion model [7]. Hegedüs and Elliott conducted *ab initio* molecular dynamics (AIMD) simulations of the amorphous-to-cubic phase transition in a 63-atom $Ge_2Sb_2Te_5$ (GST225) system and found that the fast crystallization of a-GST was caused by the excessive formation of fourfold rings by melt quenching [8]. The growth rate of a GST crystal domain is also fast, ranging $10^{-9} \sim 3$ m/s, depending on the annealing temperature [9,10]. Lee and Elliott [11] demonstrated, through an AIMD annealing simulation of a 180-atom a-GST system, that vacancies located near amorphous-crystal interfaces may promote the rapid growth of a crystal domain. Recently, the change in electronic structure by crystallization was investigated using the maximally localized Wannier function method from a large-scale AIMD simulation of a 328-atom system [12]. The complex configuration of Wannier electrons in a-GST, including many weak bonding states and lone-pair electrons, is advantageous for the fast structural transition accompanied by frequent bond-breaking and formation processes [12].

The a-GST structures build *s-p* hybridized covalent bonding states, while well-ordered crystalline structures build directional *p*-orbital resonant bonding states, which leads to a stark optical contrast between the two structures [13]. The directional p bonding could become unstable against sp^3 bonding as the *p*-bonding chain length increases [14]. A signature of the *p*-bonding instability is the softening of specific phonon modes, resulting in the distortion observed in α-GeTe with alternating long and short bonds [15]. In this sense, the

*jhish@postech.ac.kr

presence of vacancies can stabilize the p-bonding chains, and their distribution is a key for understanding the structural and electronic properties of c-GST.

The distribution of vacancies in c-GST can be either random or ordered to a certain degree [16]. The vacancy-ordered-cubic (VOC) structures slightly differ from the hexagonal structures in terms of interlayer distance and stacking geometry of Te-Te van der Waals (vdW) layers [16]. A typical hexagonal structure obtained by annealing is the Matsunaga phase, which is similar to the Kooi phase but with numerous substitutional defects of Ge and Sb atoms [17]. A major structural change in the cubic-to-hexagonal phase transition is thus accompanied by vacancy ordering. The electrical resistance of crystalline GST, which varies over a 1000-fold range, reflects vacancy ordering and exhibits a feature of the metal-insulator transition at a certain threshold [4]. Additionally, GST-based phase-change memories show a reduction in crystallization temperature and electrical resistance with an increase in operation cycles [10]. A non-Arrhenius crystallization of a-GST was observed, as the activation energy underwent a discontinuous sixfold magnitude change at $T \sim 480$ K [10]. All these observations in phase-change memories are likely attributed to the distribution of vacancies and their ordering. However, they cannot be tracked atomistically by measurements or by first-principles simulations due to their complexity in length and timescales.

The atomic-scale studies of GST on electronic and structural properties require a substantial size in atomic number and simulation time. Direct AIMD simulations are limited to ~1000 atoms due to high computational costs [18–22]. Recently, machine learning potential methods have expanded the simulation capacity to an unreachable scale by AIMD, allowing atomistic calculations with an accuracy of first-principles methods [23–26]. The medium-range order of large-sized ring configurations has been identified and the first sharp diffraction peak of x-ray structure factor in measurement has been reproduced [23]. The midgap states in amorphous GST225 [24] and quench-rate dependent crystallization [25] have also been directly addressed in machine learning potential molecular dynamics (MLMD) without resorting to phenomenological modeling. In this study, we used MLMD methods to simulate the thermal annealing of c-GST at 700 K and analyzed the distribution and rearrangement of vacancies.

II. METHODS

A. $Ge_2Sb_2Te_5$ potential

We utilized the Neural E(3)-equivariant interatomic potentials (NEQUIP) model to develop machine learning potentials (MLPs) for GST225 [27]. NEQUIP is based on graph neural networks and learns a high-dimensional potential-energy surface by partitioning the potential energy of a system into individual atomic contributions, namely atomic energies [27]. The NEQUIP process involves multiple iterations of message passing to effectively convey nonlocal structural information [27]. The message passing operates with feature tensors that contain structural information and are equivariant under rotation, reflection, and translation transformations [27].

The NEQUIP potential was constructed with a local cutoff radius r_c of 4 Å, including 7.40 atoms on average inside a local environment sphere. The maximum rotation order $l_{\max}$ of the feature tensors was set to be 3, as the potentials with $l_{\max} = 3$ reproduce the angular distribution function of liquid GST225 at 1100 K better than those with $l_{\max} = 2$ (see Supplemental Material for further information on the NEQUIP training parameters [28]). The converged GST225 potentials yielded an energy root-mean-square error (RMSE) of 51.8 meV per atom and a force RMSE of 74.7 meV/Å for the whole validation dataset. We note that the RMSE values can vary consequentially for each class of the training dataset. For the c-GST dataset, which is the primarily focused phase of this study, the RMSEs are 33.8 meV per atom for energies and 43.8 meV/Å for forces (see Supplemental Material for the validation of the GST225 potential [28]). Inclusion of a dataset in a wider energy window inevitably increases the RMSEs but covers the potential-energy surface more broadly, ensuring more vigorous stability of molecular dynamics simulations [37].

The resulting GST225 potentials simulated properly the melting and crystallization processes (see Supplemental Material for the potential-energy change during melting and crystallization [28]). The melting point of c-GST in our simulation was found to be ~1000 K, which is comparable to the measurement of ~900 K [38]. A slight discrepancy may be attributed to some factors neglected in our simulations such as surfaces or structural defects that accelerate the melting process. The amorphous-to-cubic crystallization time was estimated to be about 400 ~ 700 ps, which is similar to the results in previous studies (400 ~ 600 ps) using a different type of MLP [23].

B. Randomized atomic-system generator

To develop the GST225 potentials, we constructed a training dataset using the Randomized Atomic-system Generator (RAG) method [37]. The RAG is an approach for creating a quality training set for MLPs [37]. While AIMD simulations provide reliable data, they are limited in covering the diverse atomic configurations and thermodynamic ensembles of the potential-energy surfaces [37]. In contrast, simple random sampling probes a wide range of configurations but overlooks local minima with unphysical overweighting on high-energy configurations [37]. The RAG method overcomes these limitations by utilizing the advantages of random sampling and structural optimization from both approaches.

The RAG method generates the initial structures from randomized lattice structures, species arrangements, and atomic displacements. These initial structures from the RAG sampling are then optimized through 10 ~ 15 iterative steps of force minimization by density-functional theory (DFT) calculations, resulting in a training set that encompasses a wide spectrum of potential-energy states. The resultant RAG dataset covers a broad potential surface, including local minima, which are likely to be missed by AIMD or simple random sampling. Since the RAG scheme constructs efficiently a diverse and comprehensive training set for MLPs, it is particularly useful for complex systems such as liquids, amorphous solids, and defective crystals with less computational loads than AIMD construction.

The GST225 RAG dataset comprised 66 457 atomic configurations, covering a broad range of structural phases (liquid, amorphous solid, metastable cubic, and hexagonal)

with potential energies ranging $-4.2 \sim -3$eV per atom (see Supplemental Material for further information on the RAG dataset and its potential-energy plot [28]). Approximately 5% (3457 configurations) of the RAG dataset was randomly selected to form the validation set, and the remaining ∼95% (63 000 configurations) constituted the training set.

Our RAG training dataset encompasses an extensive array of configurations, including single elements (Ge, Sb, Te), binaries (GeTe, Sb_2Te_3), and ternaries, along with a variety of segregated structures, covering a diverse range of stoichiometries and structures. This breadth is validated through t-distributed stochastic neighbor embedding (t-SNE) analysis [37], which visualizes data distribution by reducing nonprimal dimensionalities using the similarity check [39]. Extrapolation capability of MLPs across various stoichiometries was also demonstrated in a recent study of GST compounds [40].

C. Linear chain of *p* bonding

We employed the linear chain of *p*-bonding (*p*-bonding chain) model to analyze the structure of c-GST [14]. From a stoichiometric perspective, the *p*-bonding network in GeTe is simple, with a formula unit of GeTe possessing 6 valence *p* electrons and their p_x, p_y, and p_z orbitals tending to align in a linear chainlike structure. In contrast, Sb_2Te_3 features a vdW-gapped structure with successive stacking of quintuple layers, containing 18 *p* electrons in a formula unit. This stoichiometric interpretation applies to various chemical compositions of the pseudobinary compounds $(GeTe)_m$-$(Sb_2Te_3)_n$.

The *p*-bonding chain of c-GST in this study was defined as the sequential bonding of cations and anions with restricted bonding connections that are less than 4 Å in length and larger than 135° in dihedral angle. The first peak of the radial distribution function (RDF) of c-GST at 700 K terminates at 4 Å (see Supplemental Material for the RDF and angular distribution function (ADF) of c-GST at 700 K [28]). Every linear *p*-bonding chain in c-GST is truncated by two vacancies, and its length is measured by the number of *p*-bonding units or equivalently by subtracting one from the number of constituent atoms. Notably, the structural network of *p*-bonding chains is fully determined by vacancy distribution, and thus its distribution can serve as a gauge of the vacancy ordering.

D. Vibrational density of states

The dynamical state of a simple harmonic oscillator can exhibit autocorrelation. Even when the dynamical phase of an oscillator stochastically collapses due to its finite lifetime, autocorrelation can still be picked for a large ensemble. The density of the vibrational states of the oscillators can be calculated by Fourier transforming the velocity autocorrelation functions,

$$g(\omega) = \frac{1}{N}\sum_{j}^{N}\int_{-\infty}^{\infty} dt\; e^{i\omega t}\; \gamma_j(t), \tag{1}$$

$$\gamma_j(t) = \frac{\langle \mathbf{v}_j(t+\tau)\cdot\mathbf{v}_j(\tau)\rangle_\tau}{|\mathbf{v}_j(\tau)|^2_\tau}, \tag{2}$$

where $g(\omega)$ is the vibrational density of states (VDOS) for N atoms, $\gamma_j(t)$ is the atomic velocity autocorrelation function (VACF), $\mathbf{v}_j(t)$ is the velocity vector of atom j, and $\langle\ \rangle_\tau$ represents the ensemble average over τ [41,42]. A long (>10 ps) and large (>1000 atoms) simulation is necessary to obtain a reliably converged VDOS. The frequency shift and linewidth broadening of phonons caused by their anharmonicity can be effectively captured by classical MD simulations. This method provides a reliable distribution of vibrational modes at temperatures above the Debye temperature T_D, as guaranteed by the energy equipartition theorem [41]. We note that the VACF captures not only phonons but also localized atomic vibration modes.

The VDOS of typical crystalline solids is proportional to ω^2 at low frequencies according to the Debye model. The reduced VDOS, $g(\omega)/\omega^2$, is used to investigate the low-frequency dynamics that determines the thermal transport properties. For perfect crystals, no peaks appear in the reduced VDOS below the frequency of a Brillouin peak, which originates from Van Hove singularity by the transverse acoustic (TA) phonons near the Brillouin-zone boundaries [43]. In contrast to the Brillouin peaks, there may exist another kind of peak in the VDOS spectrum below the Brillouin peaks in amorphous solids. These peaks are called boson peaks and are known to originate from structural disorder [43,44], low mechanical rigidity [45], or low atomic density [46].

E. DFT calculations

The potential energies and forces of the RAG configurations were calculated using the Vienna *Ab initio* Simulation Package (VASP) with the projector augmented-wave method [47,48]. The Perdew-Burke-Ernzerhof functional was adopted for the exchange-correlation term [49], and the DFT-D3 method with Becke-Johnson damping function was used to account for additional van der Waals energy correction [50,51]. The cutoff energy for the plane-wave basis set was set to 520 eV, and momentum space sampling was performed with an isotropic spacing of 0.13 $Å^{-1}$. We note that structural parameters can be affected by the choice of pseudopotentials [52–54]. In particular, there is a long history that electronic and structural properties are sensitive to the way that semicore *d* orbitals are treated in pseudizing as valence or core states. Also, the type of exchange-correlation functional and treatment of long-range dispersion interaction may affect the total energy and the forces, and resultingly the training dataset [23,55]. Thus, care must be taken to construct the training dataset that represents structural features properly. Otherwise, unphysical consequences such as wrong bonds, under- or overestimation of structural orders may result. The atomic configurations were visualized using the Atomic Simulation Environment (ASE) package [56].

III. RESULTS

A. Vacancy ordering during annealing

The annealing of c-GST was simulated to investigate the rearrangement of cations and vacancies. The initial atomic configuration in the annealing simulation was randomly generated by RAG [Fig. 1(a)]. Our GST225 potentials reproduced successfully the c-GST structure through direct crystallization simulation from a melt-quenched amorphous structure.

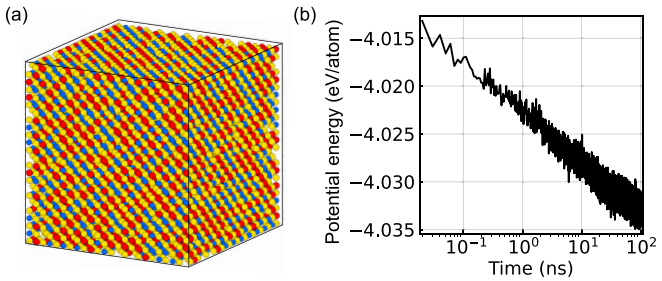

FIG. 1. (a) The initial RAG configuration of c-GST and (b) the potential-energy change during the annealing at 700 K. The balls in blue, red, and yellow in (a) correspond to Ge, Sb, and Te atoms, respectively.

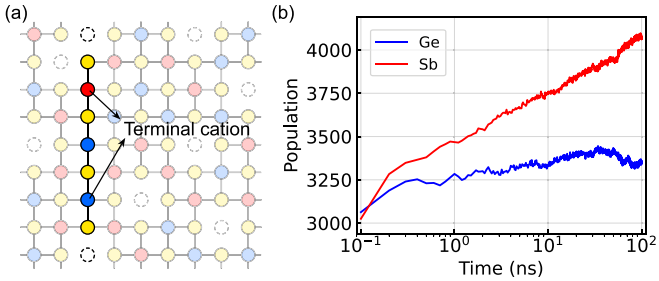

FIG. 2. (a) Schematic illustration of the terminal cation and (b) changes in terminal-cation site population. In (a), colored circles represent atoms and dashed circles denote vacancies. The set of highlighted atoms in (a) comprises the p-bonding chain of length 6 truncated by two vacancies. The population in (b) refers to the number of atoms occupying the terminal-cation sites (Ge: blue, Sb: red) as a function of the annealing time on a logarithmic scale (all time points are shifted by 100 ps).

The resulting structure was polycrystalline, exhibiting many domain walls. To focus on the vacancy-ordering analysis, we chose the RAG-generated structure as an initial configuration for the c-GST annealing simulation. We verified that the RAG configuration contains local structures similar to the directly crystallized configuration and that the main conclusion in our simulations is not affected by the choice of initial c-GST configurations (see Supplemental Material for the crystallization of melt-quenched a-GST, the comparison of the c-GST structures constructed by RAG and direct crystallization simulation, and the structure and VDOS of c-GST directly crystallized from a-GST [28]). The initial RAG configuration was the $12 \times 12 \times 12$ supercell of the rocksalt face-centered-cubic conventional cell, with 13824 lattice points in total. All 6912 anion sublattices were occupied by Te atoms, while the remaining 6912 cation sublattices were occupied by 2765 Ge, 2765 Sb, and 1382 vacancies at random. The cubic box was $\sim$72.17 Å in size and had a mass density consistent with the experimentally measured value of c-GST $\sim$6.27 g/cm^3, or equivalently $\sim$0.0331 atom per Å^{-3} [57]. The annealing simulation was carried out using the isothermal-isochoric (NVT) ensemble at 700 K, at which the crystal growth rate is reported to be the highest [9]. After a 100-ns annealing simulation, the c-GST system was transformed into a vacancy-semiordered cubic state with the potential energy lowered by 20 meV per atom [Fig. 1(b)].

The changes in atomic structures were not noticed from RDF and ADF comparison (see Supplemental Material for the comparison of partial RDFs and total ADFs of c-GST annealed for 10 ps and 100 ns [28]). In order to investigate the structural changes caused by annealing, we monitored the population of cations at the terminal-cation sites of the p-bonding chains (Fig. 2). The terminal-cation sites were occupied by Ge and Sb atoms at the same rate in the initial RAG configuration, but Sb atoms gradually outnumbered Ge atoms by annealing [Fig. 2(b)]. After 100 ns of annealing, the number of Ge and Sb atoms occupying the terminal-cation sites were 3357 and 4073, respectively, which is an excess population of Sb by $\sim$21%. The formation of Sb-Te-vacancy configurations is a key structural change toward the hexagonal Kooi phase, in which p-bonding chains always have Sb atoms at their terminal-cation sites. As the vacancies became ordered, the number of p-bonding chains increased, as did the population of Ge and Sb atoms at terminal-cation sites [Figs. 2(b) and 3(c)]. We point out that a p-bonding chain of length 2 has only one terminal-cation site.

The change in the number and length distribution of the p-bonding chains during annealing was investigated (Fig. 3). In an infinitely large virtual c-GST with randomly distributed cations and vacancies, the length distribution of the p-bonding chains converges to $\mathrm{P}(l) = x(1-x)^{l/2}$, where x is the ratio of vacancies to cation sites, and l is the length of the p-bonding chain. For cubic GST225, $x = 0.2$ and the distribution of p-bonding chain lengths follows the power law

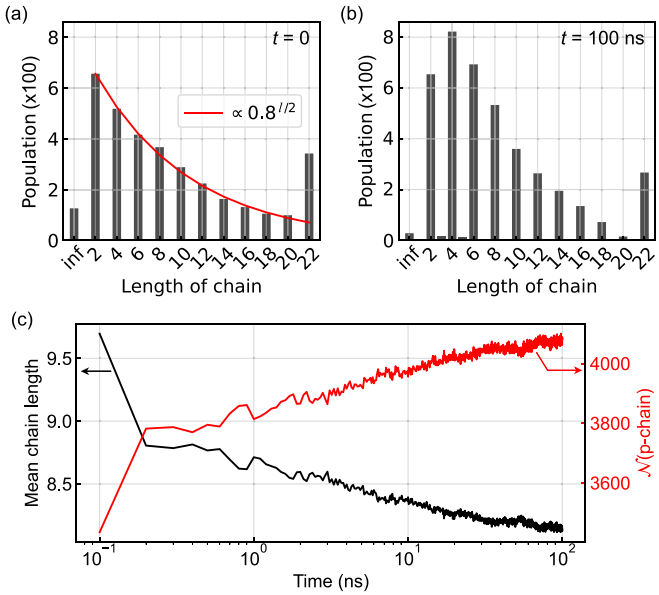

FIG. 3. The p-bonding chain length histogram at (a) $t = 0$ and (b) 100 ns. The x-tick label "inf" indicates an infinitely long p-bonding chain due to the open boundary condition, i.e., a p-bonding chain of length 24 with the chain ends interconnected over the cell. The fitting curve in red in (a) is $\sim 0.8^{l/2}$ with l as the chain length. The sum of all p-bonding chain lengths remains almost constant in the range of 33100 $\sim$ 33300. (c) The change in the mean p-bonding chain length (black curve) and the number of p-bonding chains (red curve).

$P(l) \propto 0.8^{l/2}$. The initial RAG configuration of a finite size with periodic boundary conditions shows a good fit to the power-law distribution of p-bonding chain lengths [Fig. 3(a)]. After annealing, the number of p-bonding chains with lengths >16 decreased, while the number of the p-bonding chains with lengths $4 \sim 14$ increased [Fig. 3(b)]. The total number of the p-bonding chains increased while the average length of the p-bonding chains decreased to 8.14 by annealing [Fig. 3(c)]. The vacancy-ordered configurations in the VOC and hexagonal Kooi phases of GST225 consist only of p-bonding chains of length 8.

We defined the position of vacancies to investigate their distribution and migration. Since vacancies in c-GST are not naturally identified, we defined their positions through the following steps. First, we created an excessive number of vacancy candidates at the 3-Å prolonged positions along all the p-bonding chains. These candidates were then grouped into thousands of sets, following the rule that two vacancy candidates belong to the same set if their intervacancy-candidate distance is less than 2.2 Å. By regarding the candidates within a set as duplicates of the genuine vacancy, we determined the vacancy position as the mean position of all candidates within the set. Faulty vacancies that had any neighboring atoms closer than 2 Å were removed. We note that defining a vacancy and its position in practical c-GST structures, especially at elevated temperatures, becomes ambiguous. Despite the number of vacancies in the ideal c-GST structure being 1382, lattice distortions and atomic migrations in the actual annealing simulation at 700 K resulted in fewer vacancies: 1382, 1252, 1315, 1363, and 1373 vacancies were found at $t = 0$ s, 10 ps, 100 ps, 1 ns, 10 ns, and 100 ns, respectively. See Supplemental Material for an example of the vacancy structure of c-GST [28].

The vacancy distribution was investigated using RDF and ADF of vacancies (Fig. 4). The cutoff distance for the vacancy ADF calculation was 5.2 Å, which encompasses the first peak of the vacancy RDF. In the initial RAG configuration without any atomic displacement from the ideal c-GST lattice points, the sharp peaks were observed in the vacancy RDF at $\sim 3\sqrt{2}$ Å, 6 Å, $3\sqrt{6}$ Å, and $6\sqrt{2}$ Å, and in the vacancy ADF at $\sim 60°$, $90°$, $120°$, and $180°$ [Fig. 4(a)]. Among the vacancy-RDF and ADF peaks, the 6-Å and $90°$ peaks cannot exist in the vacancy fully ordered configurations of the VOC and hexagonal phases. Throughout the annealing process, the intensities of the 6-Å and $90°$ peaks were gradually reduced by the rearrangement of vacancies (Fig. 4). This reduction in the intensities of these two peaks is evidence of local vacancy ordering in the layers along the (111) direction.

To analyze the increase in the vacancy-RDF first-peak intensity at $3\sqrt{2}$ Å and the reduction of the vacancy-RDF second-peak intensity at 6 Å in a more specific way, the peak areas were calculated. The mean coordination number of vacancy-vacancy (V-V) duos can be calculated by integrating the vacancy-RDF first peak (Fig. 4) ranging from 3.5 to 5.2 Å, weighted by the area of a sphere $4\pi r^2$ times the vacancy number density ~ 0.00368 /Å^3 [Fig. 5(a)]. A vacancy located at a cation lattice site in c-GST has 12 first-nearest cation sites at a distance of $3\sqrt{2}$ Å. The expectation number of the V-V duos is 2.4 for the vacancy-disordered configurations, while it is 6 for the vacancy fully ordered configurations. The

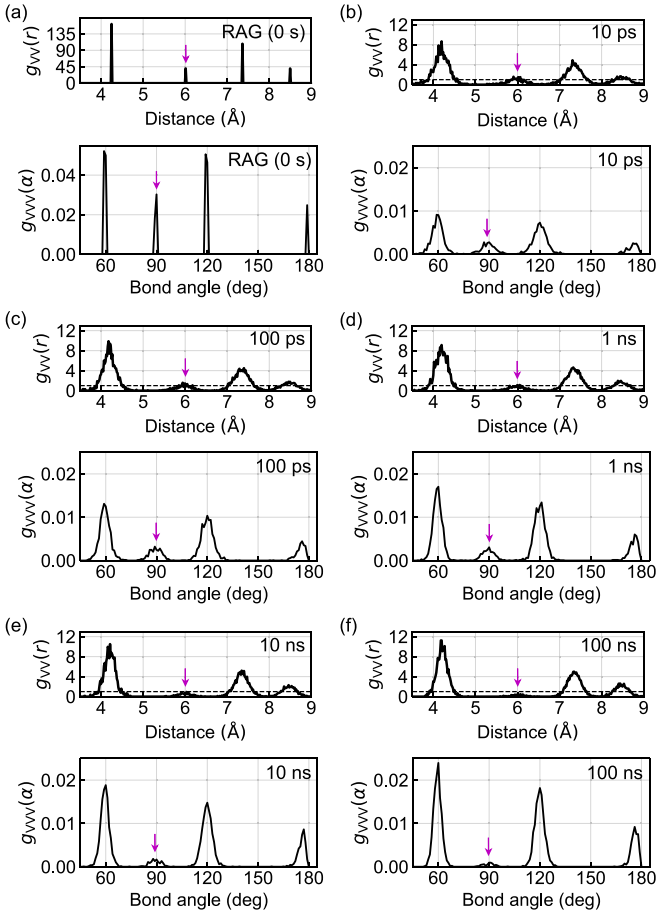

FIG. 4. Vacancy radial distribution function (g_{VV}) and vacancy angular distribution function (g_{VVV}) for (a) 0-s, (b) 10-ps, (c) 100-ps, (d) 1-ns, (e) 10-ns, and (f) 100-ns configurations, respectively. The purple arrows indicate the peaks that should disappear in the vacancy fully ordered configurations.

number of V-V duos gradually increased from 2.44 to 2.70 by annealing [Fig. 5(a)].

The vacancy-RDF second peak at 6 Å originates from the straight vacancy-Te-vacancy (V-Te-V) trio illustrated in the inset of Fig. 5(b). The number of V-Te-V trios is calculated by integrating the vacancy-RDF second peak [Fig. 5(b)] ranging from 5.3 to 6.6 Å. Since a vacancy has 6 first-nearest Te atoms at a distance of 3 Å, the average coordination number of V-Te-V trios converges to 1.2 for randomly disordered vacancies. The coordination number of the trios decreased monotonically from 1.2 to 0.2 during the 100-ns annealing process [Fig. 5(b)].

The increase in the V-V duo coordination by $\sim 11\%$ and the reduction of V-Te-V trio coordination by $\sim 83\%$ serve as evidence of vacancy ordering towards planar vacancy layers. For example, when a Te atom neighbors one vacancy in a direction (e.g., x axis), the Te atom tends to simultaneously neighbor other vacancies in the other directions (e.g., y- and z axes). On the other hand, a situation in which a Te atom neighbors two vacancies in a single direction on both sides is extremely unfavorable.

Migration of a vacancy is equivalent to the positional exchange of a vacancy with a neighboring cation. To determine

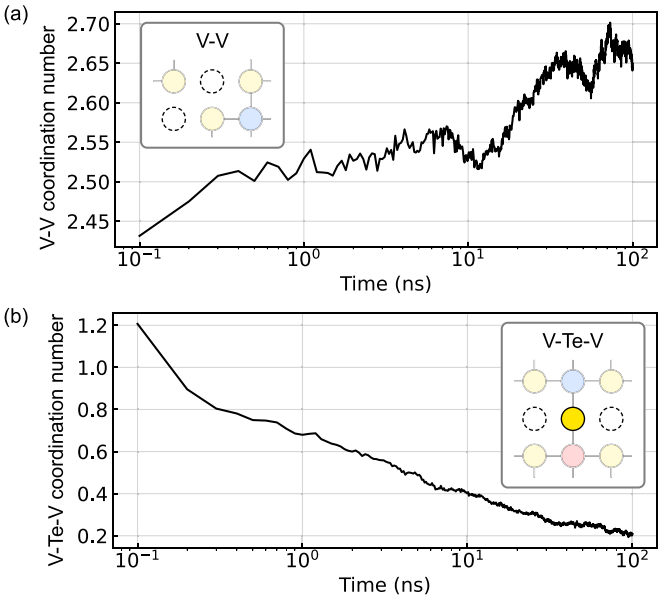

FIG. 5. Change in the number of (a) V-V duos and (b) straight V-Te-V trios during annealing. The insets illustrate examples of the V-V duo and V-Te-V trio configurations. The annealing time is given on a logarithmic scale shifted by 100 ps.

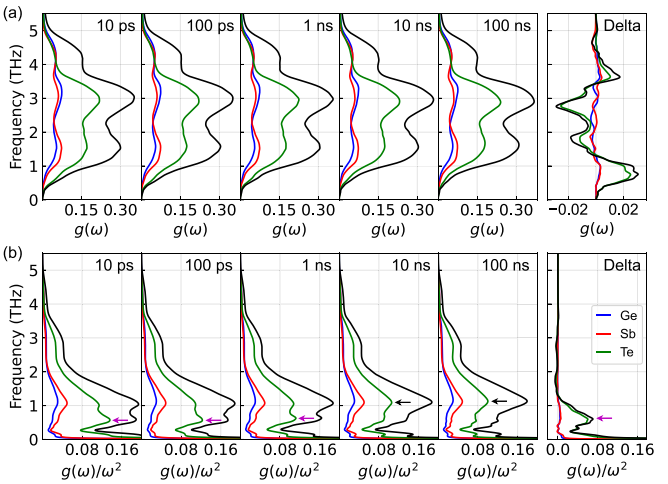

FIG. 7. Partial VDOS of c-GST thermally annealed for 10 ps, 100 ps, 1 ns, 10 ns, and 100 ns. The reduced VDOS in (b) is scaled by ω^{-2} from the VDOS in (a). The rightmost panel labeled "Delta" shows the subtraction of VDOS at 10 ps by that at 100 ns. The arrows in purple highlight the distinct boson peaks and those in black the Brillouin peaks. All curves are smeared by Gaussians with a 0.05-THz width.

whether Ge or Sb is more responsible for vacancy migration, we calculated the mean-squared displacement (MSD) from the initial RAG configuration during annealing. See Supplemental Material for the specieswise MSD along the annealing [28]. During the first 1 ns, the MSD of Sb atoms increased more rapidly and became larger than the MSD of Ge by 0.5 Å^2. The MSD gap between Ge and Sb remained $\sim$0.5 Å^{-1} after 1 ns, indicating that Ge and Sb atoms equally contributed to vacancy migration. Despite having a smaller covalent radius (1.21 Å) and lighter mass (72.64 a.u.) than Sb (covalent radius of 1.40 Å and mass of 121.76 a.u.), Ge did not contribute more to vacancy migration than Sb.

B. Debye-Waller thermal *B* factor

The Debye-Waller thermal isotopic factor $B_{\rm iso} = \frac{8\pi^2}{3}\langle u^2\rangle$ was calculated at five time points (10 ps, 100 ps, 1 ns, 10 ns, and 100 ns), where $\langle u^2\rangle$ is the mean squared displacement of ions (Fig. 6). We obtained $B_{\rm iso}$ at each time point with a 100-ps-long, 300 K, *NVT*-MD simulation followed by a 50-ps-long thermal equilibration. The mean thermal factors of Ge, Sb, and Te decreased monotonically until 100 ns. Notably, the mean thermal factor of Te atoms $B^{\rm Te}_{\rm iso}$ decreased significantly by $\sim$19% (from $B^{\rm Te}_{\rm iso} = 1.58$ Å^2 at 10 ps to $B^{\rm Te}_{\rm iso} = 1.29$ Å^2 at 100 ns). The vacancy disorder in the initial RAG configuration seem responsible for the abnormally large thermal factor of Te atoms. The thermal factors of c-GST measured by neutron- and x-ray diffraction at room temperature were $B^{\rm Ge}_{\rm iso} = 1.63$ Å^2, $B^{\rm Se}_{\rm iso} = 1.64$ Å^2, and $B^{\rm Te}_{\rm iso} = 1.671$ Å^2 [58]. The mean thermal factor $B_{\rm Te} = 1.58$ Å^2 of the configuration annealed for 10 ps is close to the measurement.

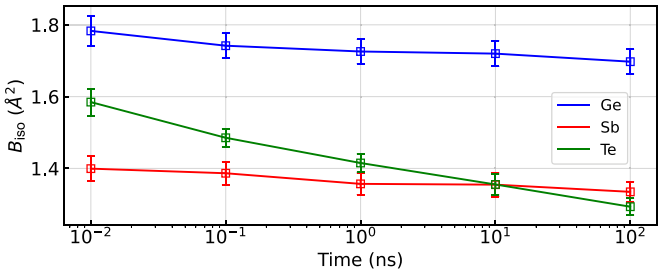

FIG. 6. Change in $B_{\rm iso}(T = 300$ K) by annealing. The error bars indicate the standard deviation of the thermal factors calculated from equilibrium MD simulations.

The sensitivity of $B^{\rm Te}_{\rm iso}$ to annealing suggests that the vacancy distribution significantly affects the dynamics of Te lattices. This result is convincing from our finding that vacancies are always surrounded by the nearby Te atoms. It also implies that the thermal *B* factor of Te atoms could potentially serve as an indicator of the degree of vacancy ordering.

C. Boson peak

We calculated the VDOS of c-GST to analyze its dynamic states through vacancy ordering (Fig. 7). The VDOSs were calculated from the VACF of the same 300 K *NVT*-MD simulations used to calculate the thermal factors. The change in the overall shape of the VDOS is negligible, except for the localized vibration modes at $\sim$0.575 THz. These localized modes are more clearly recognized in the reduced VDOS as scaled by ω^{-2} [Fig. 7(b)], forming a so-called boson peak. The VDOS of the configurations at 10 ps, 100 ps, and 1 ns show distinctive boson peaks, while those at 10 and 100 ns do not. Notably, the boson peak modes involve the vibration of Te atoms. Another peak at $\sim$1.1 THz [Fig. 7(b)] is the Van Hove singularity developed by the TA phonon modes at the zone boundaries, namely the Brillouin peak. We found that

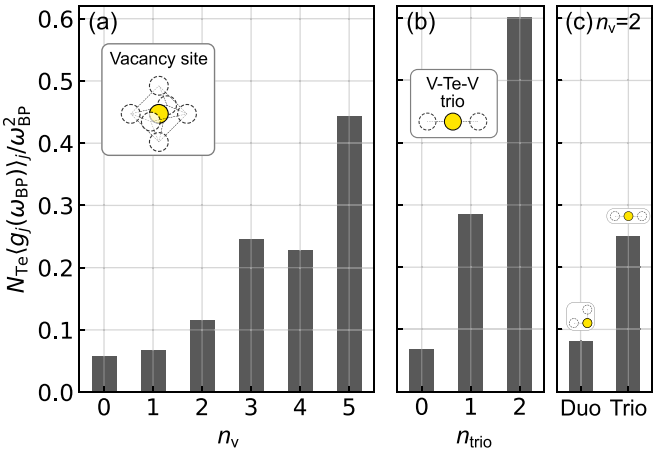

FIG. 8. Correlation between the vacancy distribution and boson peak intensity. Configuration-averaged boson peak intensity projected into a Te atom in terms of (a) the number of vacancies (n_v) at the cation sites nearest to Te, (b) the number of straight trios (n_{trio}), and (c) the two characteristic configurations (V-V duo and V-Te-V trio) of Te atoms with two neighboring vacancies ($n_v = 2$). The boson peak intensity is scaled by the number of Te atoms N_{Te}(=6912) for comparison to the boson peak in Fig. 7.

this Brillouin peak is evenly contributed by all elements, indicating the delocalized feature of the phonon modes. A slight shift in the position of the Brillouin peak is an artifact due to the tail of the nearby boson peak. The shape of the Brillouin peak does not change as the vacancies become ordered.

The normal mode analysis for the boson peak vibrational modes showed that the boson peak consists primarily of the vibrational modes localized at Te atoms (see Supplemental Material for visualization of the atomwise boson peak intensity [28]). The boson peak intensity projected on atom j provides a strong signature of the correlation between the vacancy distribution and the boson peak. We calculated the atom-projected boson peak intensity $g_j(\omega_{BP})/\omega^2_{BP}$ from the atom-projected VDOS $g_j(\omega) = \frac{1}{3N}\sum_i \delta(\omega-\omega_i)\sum_\alpha u^2_{i,j\alpha}$, where u_i is the polarization vector of the ith vibrational normal mode, N is the total number of atoms, and $\alpha = x$, y, or z. We found that configuration-averaged value of the atom-projected boson peak intensity $g_j(\omega_{BP})/\omega^2_{BP}$ is proportional to the number of vacancies at the cation sites nearest to Te atom j [Fig. 8(a)]. Moreover, the boson peak is contributed most by Te atoms that have a specific arrangement of neighboring vacancies. In Fig. 8(b), we observe that the boson peak intensity is almost linear to the number of V-Te-V trios. This finding becomes more apparent when we compare the contribution to the boson peak from the modes localized at Te atoms with two neighboring vacancies. The contribution is large when a Te atom and two vacancies form a straight trio (V-Te-V) but, for V-V duos, it is almost the same as the case for 0 or 1 neighboring vacancy [Fig. 8(c)]. We note that the V-V duo formation is the building block for the vacancy layers (i.e., vacancy ordering) as found in the hexagonal structure.

These findings support that the disappearance of the boson peak is directly attributed to the vacancy ordering and, in other words, that the structural disorder in c-GST contributes to the development of the boson peak. The boson peak intensity in c-GST appears to be highly correlated with the large thermal factor of Te atoms. A strong correlation between boson peak modes and thermal factors was previously observed in a two-dimensional power-law potential model [44].

IV. DISCUSSION

We constructed a machine-learned GST225 potential using the RAG dataset and simulated 100-ns annealing of c-GST at 700 K. After annealing, the initial RAG configuration of c-GST with vacancy disorder transformed into a vacancy-semiordered cubic structure with a lowered energy by ∼20 meV per atom. The structural transition was captured by the p-bonding chain model and the vacancy distribution analysis. In the final vacancy-semiordered configuration, Sb atoms occupied the terminal-cation sites in the p-bonding chains 21% more frequently than Ge atoms. The number of p-bonding chains longer than 16 decreased by annealing, while the number of shorter p-bonding chains increased. The change in vacancy distribution also supports vacancy ordering. Vacancies tend to be located next to Te atoms already neighboring other vacancies, while the configuration of a straight V-Te-V trio is extremely unfavored. Our annealing simulation of 100 ns may not be long enough to achieve vacancy ordering on a full scale, but all observed structural features consistently indicate the progression of layerlike vacancy ordering.

We identified several key features accompanying the vacancy ordering. A boson peak develops at ∼0.575 THz due to the vacancy disorder at the initial stages of annealing ($t <$ 1ns) and then gradually disappears as vacancies are ordered. This formation and evolution of the boson peak by the vacancy ordering is in sheer contrast to the common observation that the boson peaks are formed in amorphous materials. The abnormal boson peak in c-GST is attributed to the modes at Te atoms with certain but energetically unfavorable configurations, while the lattice structure retains the cubic symmetry. We note that such a dynamical phase transition without a change in the density or symmetry of the lattice structure is a unique feature of c-GST. The Debye-Waller thermal B factor of Te decreased by ∼19% in the vacancy-semiordered cubic phase, indicating its correlation with the boson peak suppression. The observable response of the thermal factor and the boson peak suggests that they can serve as dynamic indicators of the vacancy ordering. Controlling the localized boson peak modes by the vacancy ordering can be an efficient tool for manipulating the thermoelectric properties of the chalcogenides. Our findings by large-scale MLMD simulations provide a microscopic understanding of the vacancy ordering, which can be utilized for developing multilevel memories and neuromorphic devices using phase-change materials.

The RAG dataset-trained $Ge_2Sb_2Te_5$ potential in LAMMPS pair-potential format (RAG_GST225_potential.pb, 2.5 MB) is available [59]. The RAG configuration dataset and other data supporting the findings of this study and the computational tools (simulation script and analysis codes) used in this study are available from the corresponding author upon reasonable request.

ACKNOWLEDGMENTS

This study was supported by the National Research Foundation of Korea (NRF) Grant No. 2022R1A2C1006530 funded by the Korea government (MSIT), and by Samsung Electronics Co., Ltd. (Grant No. IO201214-08146-01). Supercomputing resources including technical support were provided by Supercomputing Center, Korea Institute of Science and Technology Information (Contract No. KSC-2022-CRE-0366).

[1] M. Wuttig and N. Yamada, Phase-change materials for rewriteable data storage, Nat. Mater. **6**, 824 (2007).

[2] S. Raoux and M. Wuttig, *Phase Change Materials* (Springer, New York, 2009).

[3] G. W. Burr, M. J. Breitwisch, M. Franceschini, D. Garetto, K. Gopalakrishnan, B. Jackson, B. Kurdi, C. Lam, L. A. Lastras, A. Padilla *et al.*, Phase change memory technology, J. Vac. Sci. Technol. B **28**, 223 (2010).

[4] T. Siegrist, P. Jost, H. Volker, M. Woda, P. Merkelbach, C. Schlockermann, and M. Wuttig, Disorder-induced localization in crystalline phase-change materials, Nat. Mater. **10**, 202 (2011).

[5] N. Yamada and T. Matsunaga, Structure of laser-crystallized $Ge_2Sb_{2+x}Te_5$ sputtered thin films for use in optical memory, J. Appl. Phys. **88**, 7020 (2000).

[6] B. J. Kooi and J. T. M. De Hosson, Electron diffraction and high-resolution transmission electron microscopy of the high temperature crystal structures of $Ge_xSb_2Te_{3+x}$ (x = 1,2,3) phase change material, J. Appl. Phys. **92**, 3584 (2002).

[7] A. V. Kolobov, P. Fons, A. I. Frenkel, A. L. Ankudinov, J. Tominaga, and T. Uruga, Understanding the phase-change mechanism of rewritable optical media, Nat. Mater. **3**, 703 (2004).

[8] J. Hegedüs and S. R. Elliott, Microscopic origin of the fast crystallization ability of Ge–Sb–Te phase-change memory materials, Nat. Mater. **7**, 399 (2008).

[9] J. Orava, A. L. Greer, B. Gholipour, D. W. Hewak, and C. E. Smith, Characterization of supercooled liquid $Ge_2Sb_2Te_5$ and its crystallization by ultrafast-heating calorimetry, Nat. Mater. **11**, 279 (2012).

[10] R. Jeyasingh, S. W. Fong, J. Lee, Z. Li, K.-W. Chang, D. Mantegazza, M. Asheghi, K. E. Goodson, and H. S. P. Wong, Ultrafast characterization of phase-change material crystallization properties in the melt-quenched amorphous phase, Nano Lett. **14**, 3419 (2014).

[11] T. H. Lee and S. R. Elliott, Structural role of vacancies in the phase transition of $Ge_2Sb_2Te_5$ memory materials, Phys. Rev. B **84**, 094124 (2011).

[12] T. H. Lee and S. R. Elliott, The relation between chemical bonding and ultrafast crystal growth, Adv. Mater. **29**, 1700814 (2017).

[13] K. Shportko, S. Kremers, M. Woda, D. Lencer, J. Robertson, and M. Wuttig, Resonant bonding in crystalline phase-change materials, Nat. Mater. **7**, 653 (2008).

[14] Y.-S. Song and S.-H. Jhi, Effect of vacancy disorder in phase-change materials, J. Phys.: Condens. Matter **32**, 175401 (2020).

[15] Y.-S. Song, J. Kim, and S.-H. Jhi, Phonon instability and broken long-ranged *p* bond in Ge-Sb-Te phase-change materials from first principles, Phys. Rev. Appl. **9**, 054044 (2018).

[16] B. Zhang, X.-P. Wang, Z.-J. Shen, X.-B. Li, C.-S. Wang, Y.-J. Chen, J.-X. Li, J.-X. Zhang, Z. Zhang, S.-B. Zhang *et al.*, Vacancy structures and melting behavior in rock-salt GeSbTe, Sci. Rep. **6**, 25453 (2016).

[17] T. Matsunaga, N. Yamada, and Y. Kubota, Structures of stable and metastable $Ge_2Sb_2Te_5$, an intermetallic compound in GeTe-Sb_2Te_3 pseudobinary systems, Acta Crystallogr. B: Struct. Sci. Cryst. Eng. Mater. **60**, 685 (2004).

[18] T. H. Lee and S. R. Elliott, *Ab initio* computer simulation of the early stages of crystallization: Application to $Ge_2Sb_2Te_5$ phase-change materials, Phys. Rev. Lett. **107**, 145702 (2011).

[19] J. Kalikka, J. Akola, J. Larrucea, and R. O. Jones, Nucleus-driven crystallization of amorphous $Ge_2Sb_2Te_5$: A density functional study, Phys. Rev. B **86**, 144113 (2012).

[20] I. Ronneberger, W. Zhang, H. Eshet, and R. Mazzarello, Crystallization properties of the $Ge_2Sb_2Te_5$ phase-change compound from advanced simulations, Adv. Funct. Mater. **25**, 6407 (2015).

[21] J. Kalikka, J. Akola, and R. O. Jones, Crystallization processes in the phase change material $Ge_2Sb_2Te_5$: Unbiased density functional/molecular dynamics simulations, Phys. Rev. B **94**, 134105 (2016).

[22] I. Ronneberger, W. Zhang, and R. Mazzarello, Crystal growth of $Ge_2Sb_2Te_5$ at high temperatures, MRS Commun. **8**, 1018 (2018).

[23] F. C. Mocanu, K. Konstantinou, T. H. Lee, N. Bernstein, V. L. Deringer, G. Csányi, and S. R. Elliott, Modeling the phase-change memory material, $Ge_2Sb_2Te_5$, with a machine-learned interatomic potential, J. Phys. Chem. B **122**, 8998 (2018).

[24] K. Konstantinou, F. C. Mocanu, T.-H. Lee, and S. R. Elliott, Revealing the intrinsic nature of the mid-gap defects in amorphous $Ge_2Sb_2Te_5$, Nat. Commun. **10**, 3065 (2019).

[25] F. C. Mocanu, K. Konstantinou, and S. R. Elliott, Quench-rate and size-dependent behaviour in glassy $Ge_2Sb_2Te_5$ models simulated with a machine-learned Gaussian approximation potential, J. Phys. D: Appl. Phys. **53**, 244002 (2020).

[26] Y.-X. Zhou, H.-Y. Zhang, V. L. Deringer, and W. Zhang, Structure and dynamics of supercooled liquid $Ge_2Sb_2Te_5$ from machine-learning-driven simulations, Phys. Status Solidi RRL **15**, 2000403 (2021).

[27] S. Batzner, A. Musaelian, L. Sun, M. Geiger, J. P. Mailoa, M. Kornbluth, N. Molinari, T. E. Smidt, and B. Kozinsky, E(3)-equivariant graph neural networks for data-efficient and accurate interatomic potentials, Nat. Commun. **13**, 2453 (2022).

[28] See Supplemental Material at http://link.aps.org/supplemental/10.1103/PhysRevMaterials.8.013606 for the details of RAG dataset and its potential energy plot; the nequip training parameters; the validation of the GST225 potential; the RDF and ADF of c-GST at 700 K; an example of the vacancy structure of c-GST; the RDF and ADF changes in annealing simulation; the specieswise mean-squared displacement along the annealing; the longitudinal and transverse decomposition of VDOSs; the examples of the atomwise intensity of the boson peak modes; the structure and VDOS of c-GST directly

crystallized from a-GST; lattice thermal conductivity calculated by Müller-Plathe reverse non-equilibrium molecular dynamics simulation. The Supplemental Material also contains Refs. [29–36].

[29] Y. M. Beltukov, C. Fusco, A. Tanguy, and D. A. Parshin, Transverse and longitudinal vibrations in amorphous silicon, J. Phys.: Conf. Ser. **661**, 012056 (2015).

[30] F. Müller-Plathe, A simple nonequilibrium molecular dynamics method for calculating the thermal conductivity, J. Chem. Phys. **106**, 6082 (1997).

[31] A. P. Thompson, H. M. Aktulga, R. Berger, D. S. Bolintineanu, W. M. Brown, P. S. Crozier, P. J. in 't Veld, A. Kohlmeyer, S. G. Moore, T. D. Nguyen *et al.*, LAMMPS - a flexible simulation tool for particle-based materials modeling at the atomic, meso, and continuum scales, Comput. Phys. Commun. **271**, 108171 (2022).

[32] P. Virtanen, R. Gommers, T. E. Oliphant, M. Haberland, T. Reddy, D. Cournapeau, E. Burovski, P. Peterson, W. Weckesser, J. Bright *et al.*, SciPy 1.0: Fundamental algorithms for scientific computing in Python, Nat. Methods **17**, 261 (2020).

[33] H.-K. Lyeo, D. G. Cahill, B.-S. Lee, J. R. Abelson, M.-H. Kwon, K.-B. Kim, S. G. Bishop, and B.-k. Cheong, Thermal conductivity of phase-change material $Ge_2Sb_2Te_5$, Appl. Phys. Lett. **89**, 151904 (2006).

[34] J. Lee, E. Bozorg-Grayeli, S. Kim, M. Asheghi, H. S. Philip Wong, and K. E. Goodson, Phonon and electron transport through $Ge_2Sb_2Te_5$ films and interfaces bounded by metals, Appl. Phys. Lett. **102**, 191911 (2013).

[35] E. K. Kim, S. I. Kwun, S. M. Lee, H. Seo, and J. G. Yoon, Thermal boundary resistance at $Ge_2Sb_2Te_5$/ZnS:SiO_2 interface, Appl. Phys. Lett. **76**, 3864 (2000).

[36] C. Peng, L. Cheng, and M. Mansuripur, Experimental and theoretical investigations of laser-induced crystallization and amorphization in phase-change optical recording media, J. Appl. Phys. **82**, 4183 (1997).

[37] Y.-J. Choi and S.-H. Jhi, Efficient training of machine learning potentials by a randomized atomic-system generator, J. Phys. Chem. B **124**, 8704 (2020).

[38] N. Yamada, E. Ohno, K. Nishiuchi, N. Akahira, and M. Takao, Rapid-phase transitions of GeTe-Sb_2Te_3 pseudobinary amorphous thin films for an optical disk memory, J. Appl. Phys. **69**, 2849 (1991).

[39] L. van der Maaten and G. Hinton, Visualizing data using t-SNE, J. Mach. Learn. Res. **9**, 2579 (2008).

[40] Y. Zhou, W. Zhang, E. Ma, and V. L. Deringer, Device-scale atomistic modelling of phase-change memory materials, Nat. Electron. **6**, 746 (2023).

[41] J. M. Dickey and A. Paskin, Computer simulation of the lattice dynamics of solids, Phys. Rev. **188**, 1407 (1969).

[42] M. T. Dove, *Introduction to Lattice Dynamics* (Cambridge University Press, Cambridge, 1993).

[43] S. Ciliberti, T. S. Grigera, V. Martín-Mayor, G. Parisi, and P. Verrocchio, Brillouin and boson peaks in glasses from vector Euclidean random matrix theory, J. Chem. Phys. **119**, 8577 (2003).

[44] Y.-C. Hu and H. Tanaka, Origin of the boson peak in amorphous solids, Nat. Phys. **18**, 669 (2022).

[45] N. Tomoshige, H. Mizuno, T. Mori, K. Kim, and N. Matubayasi, Boson peak, elasticity, and glass transition temperature in polymer glasses: Effects of the rigidity of chain bending, Sci. Rep. **9**, 19514 (2019).

[46] A. I. Chumakov, G. Monaco, A. Fontana, A. Bosak, R. P. Hermann, D. Bessas, B. Wehinger, W. A. Crichton, M. Krisch, R. Rüffer *et al.*, Role of disorder in the thermodynamics and atomic dynamics of glasses, Phys. Rev. Lett. **112**, 025502 (2014).

[47] G. Kresse and J. Furthmüller, Efficient iterative schemes for *ab initio* total-energy calculations using a plane-wave basis set, Phys. Rev. B **54**, 11169 (1996).

[48] G. Kresse and D. Joubert, From ultrasoft pseudopotentials to the projector augmented-wave method, Phys. Rev. B **59**, 1758 (1999).

[49] J. P. Perdew, K. Burke, and M. Ernzerhof, Generalized gradient approximation made simple, Phys. Rev. Lett. **77**, 3865 (1996).

[50] S. Grimme, J. Antony, S. Ehrlich, and H. Krieg, A consistent and accurate ab initio parametrization of density functional dispersion correction (DFT-D) for the 94 elements H-Pu, J. Chem. Phys. **132**, 154104 (2010).

[51] S. Grimme, S. Ehrlich, and L. Goerigk, Effect of the damping function in dispersion corrected density functional theory, J. Comput. Chem. **32**, 1456 (2011).

[52] D. Campi, L. Paulatto, G. Fugallo, F. Mauri, and M. Bernasconi, First-principles calculation of lattice thermal conductivity in crystalline phase change materials: GeTe, Sb_2Te_3, and $Ge_2Sb_2Te_5$, Phys. Rev. B **95**, 024311 (2017).

[53] J. Tominaga, A. V. Kolobov, P. Fons, T. Nakano, and S. Murakami, Ferroelectric order control of the Dirac-semimetal phase in GeTe-Sb_2Te_3 superlattices, Adv. Mater. Interfaces **1**, 1300027 (2014).

[54] G. Lee and S.-H. Jhi, *Ab initio* studies of structural and electronic properties of the crystalline $Ge_2Sb_2Te_5$, Phys. Rev. B **77**, 153201 (2008).

[55] A. Bouzid, G. Ori, M. Boero, E. Lampin, and C. Massobrio, Atomic-scale structure of the glassy $Ge_2Sb_2Te_5$ phase change material: A quantitative assessment via first-principles molecular dynamics, Phys. Rev. B **96**, 224204 (2017).

[56] A. Hjorth Larsen, J. Jørgen Mortensen, J. Blomqvist, I. E. Castelli, R. Christensen, M. Dułak, J. Friis, M. N. Groves, B. Hammer, C. Hargus *et al.*, The atomic simulation environment—a Python library for working with atoms, J. Phys.: Condens. Matter **29**, 273002 (2017).

[57] W. K. Njoroge, H.-W. Wöltgens, and M. Wuttig, Density changes upon crystallization of $Ge_2Sb_{2.04}Te_{4.74}$ films, J. Vac. Sci. Technol. A **20**, 230 (2002).

[58] S.-i. Shamoto, K. Kodama, S. Iikubo, T. Taguchi, N. Yamada, and T. Proffen, Local crystal structures of $Ge_2Sb_2Te_5$ revealed by the atomic pair distribution function analysis, Jpn. J. Appl. Phys. **45**, 8789 (2006).

[59] Y.-J. Choi, M. Ghim, and S.-H. Jhi, ZENODO: RAG GST225 potential (2024), DOI: 10.5281/zenodo.10516694.